CHEMISTRY OF MATERIALS

pubs.acs.org/cm

Article

Molecular Mechanisms of Superelasticity and Ferroelasticity in Organic Semiconductor Crystals

Hong Sun, Sang Kyu Park, Ying Diao, Eric P. Kvam,* and Kejie Zhao*

Cite This: *Chem. Mater.* 2021, 33, 1883−1892

Read Online

ACCESS | Metrics & More | Article Recommendations | Supporting Information

ABSTRACT: Flexible organic crystals enabled by cooperative phase transitions attract enormous interest in solid-state chemistry to produce light, biocompatible, and environmentally benign devices. The recently unveiled super- and ferroelastic organic semiconductor crystals provide a pathway to achieve ultraflexible single-crystal electronics. However, the mechanistic understanding of cooperative transitions in organic crystals is rather at the nascent stage, and most of such studies rely on the trial-and-error approach in molecular design. Compared to the well-studied phase transition in metallic alloys, the key challenge in understanding the organic phase transitions is the elusive crystallography involving intricate molecular dynamics and defects. Here, we leverage the phase transformation theory, genetic algorithm refined molecular modeling, and experimental validation to study the versatile cooperative transitions in bis(triisopropylsilylethynyl)-pentacene semiconductor crystals. The molecular rotation governed thermoelasticity, interconvertible super- and ferroelastic transitions, and molecular twinning are systematically studied by integrating the lattice crystallography and molecular motions. We illustrate the molecular defects of disclination dipoles and molecular stacking faults associated with the molecular twinning process. The fundamental understanding underpins the molecular mechanism of cooperative transitions in a variety of organic solids to promote a new avenue of environmentally responsive organic devices.

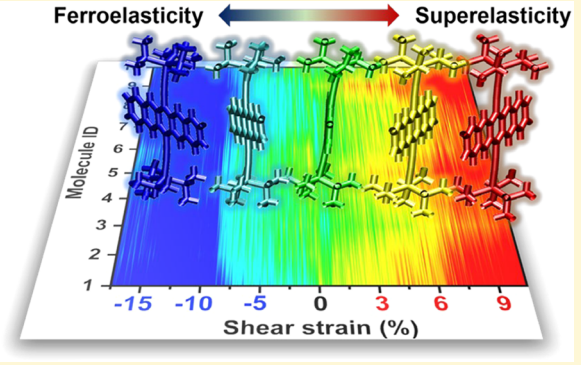

INTRODUCTION

Organic crystals were deemed still and brittle. Such a perception has been defied by the recent reports of flexible and bendable organic crystals.[1−5] The emergence of the unconventional phenomena in organic solids, such as rapid shape reconfiguration induced by heat, pressure, or light, attracts enormous interest from solid-state chemists to produce light, biocompatible, and environmentally benign devices.[6−11] The flexibility of organic crystals is generally manifested by elastic and plastic deformation. Materials subjected to elastic deformation can regain their original shape after releasing the stress while plasticity can disrupt the structure and result in irreversible deformation. Reddy et al. reported remarkable elasticity in caffeine cocrystals, which was attributed to the rearrangement of the three-dimensional weak network formed by CH−π interactions.[1] Naumov and co-workers found that the gliding of stacked molecular layers gave rise to high plasticity in hexachlorobenzene crystals.[3] More interestingly, Takamizawa et al. demonstrated the terephthalamide crystal[12] and 4,4′-dicarboxydiphenyl ether crystals[13] which can withstand large deformation while retaining structural integrity through either polymorphic transitions or lattice reorientations. Such characteristics are reminiscent of superelasticity and ferroelasticity in shape-memory alloys—in superelasticity, the daughter phase becomes unstable, and the initial mother phase reemerges upon releasing the stress,[14,15] while ferroelasticity is typically facilitated by lattice reorientation, and the structure recovers the original shape upon loading in an opposite direction.[16] Deformable organic crystals have recently sparked vast attention in crystal engineering and pharmaceutical engineering.[17−19] Nevertheless, most of those organic solids comprising simple hydrocarbon groups, albeit intriguing, are limited by their functionalities.

Molecules and polymers with extended π-conjugation warrant intensive studies in the emerging field of organic semiconductors owing to their effective charge transferability and solution processability. They are now actively pursued in the development of flexible and printed devices, such as solar cells, light-emitting diodes, field-effect transistors, sensors, wearable devices, and electronic skins.[20,21] Chung et al. reported thermoelasticity and shape memory in two molecular organic semiconductors, ditBu-BTBT and TIPS-pentacene.[22]

Received: January 9, 2021
Revised: February 4, 2021
Published: February 18, 2021

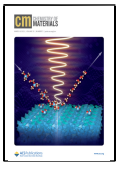

Thermally triggered rapid cooperative phase transition and associated shape and function memories were observed for both molecules within seconds. Lately, we unveiled super- and ferroelasticity in the TIPS-pentacene crystal which can tolerate a tensile strain of over 13% while maintaining the high charge carrier mobility.[23] This finding provides a pathway to achieve ultraflexible high-performance single-crystal organic electronics. To harvest the superelastic deformability in organic crystals, especially in the semiconducting organic crystals, a profound mechanistic understanding of cooperative transitions is imperative to develop principles of molecular design. In experiments, X-ray characterization and Raman spectroscopy can help examine the static crystallographic relations of different polymorphs. However, the intricate dynamics of the molecular structure during the polymorphic transitions challenges a direct experimental observation as such events occur in an extremely short time scale (usually within seconds). To this end, a molecular level understanding is desired to scrutinize the dynamic changes of the packing structure upon the cooperative transitions. By employing molecular dynamics simulations, Cuppen et al. pointed out that the local fluctuation in the conformation of the aliphatic chains gave rise to the temperature-induced polymorphic transition of DL-norleucine crystals.[17] Complementing Chuang's experimental work, Geerts et al. provided the simulation evidence of rotating side chains in the thermoelastic transition of semiconducting ditBu-BTBT materials.[22] In our recent work, we revealed that the cooperative rotational and displacive molecular motions facilitated the super- and ferroelasticity in TIPS-pentacene crystals using ab initio modeling and molecular simulation.[23] However, the concepts of "local fluctuation" and "cooperative rotational and displacive motions" are not sufficient to populate the vacant knowledge space regarding the kinetics and energetics of the thermo-, super-, and ferroelastic transitions in conjugated molecules.

Superelasticity and ferroelasticity are well documented in metallic alloys, and materials theories have been well developed to guide the design of shape memory alloys.[14,16] Although the cooperative transitions of organic solids involve complicated conformational changes due to the intricate intra- and intermolecular interactions, they share a few common features of homogeneous lattice deformation in the martensitic transitions in metals and ceramics. Here, we transfer the prior knowledge about the phase descriptor and phenomenological theories of martensitic transition in metallurgy[15] to the organic system. With the aid of genetic algorithm refined atomistic modeling (Materials and Methods), we systematically investigate the thermomechanically induced cooperative transitions in TIPS-pentacene semiconductors. Figure 1 sketches a phase diagram in the space of thermal (T-axis) and mechanical (σ–ε plane) load. The reversible polymorphic transition can be regulated by the change of temperature through thermoelasticity. The high-temperature (HT) phase transforms to the low-temperature (LT) phase via superelasticity under a shear load (σ–ε plane). The LT phase deforms through ferroelasticity and deformation twinning. Different types of superelasticity and ferroelasticity can be triggered by prescribing load in different directions. The twinned domains can also revert to their original orientation by reverse mechanical load or thermal treatment. We demonstrate for the first time the thermoelastic transition manifested by backbone rotation, the interconvertible behavior of super- and ferroelasticity, the diffusive interface in superelastic transition,

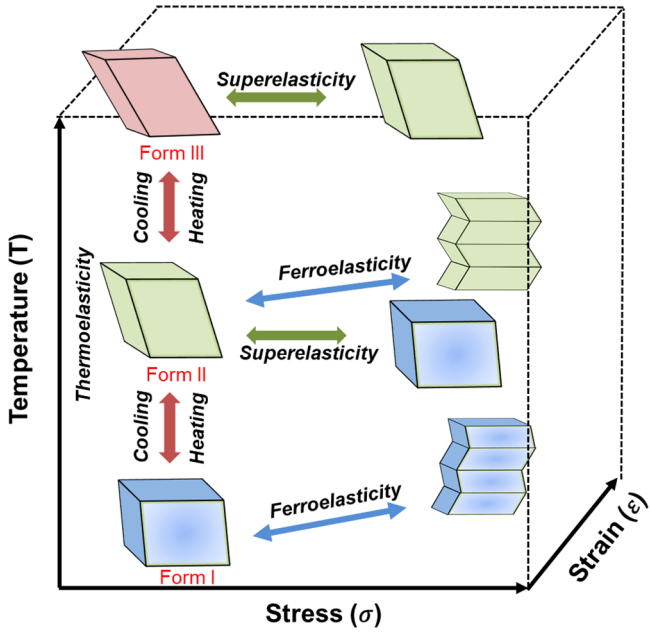

Figure 1. Sketch of the phase diagram of the TIPS-pentacene semiconductor crystal in the space of temperature–stress–strain exhibiting thermoelasticity (TE), superelasticity (SE), and ferroelasticity (FE).

and molecular defects of disclination dipoles and stacking faults in the twinning process. The theoretical framework integrating both lattice crystallography and molecular motions can find use in analyzing the mechanisms of homogeneous cooperative transitions in a variety of organic solids, especially in the conjugated semiconducting materials. The comprehensive molecular understanding will help open new avenues for rapid, reversible modulation of electronic and optical properties in organic crystals by means of molecular selection and design.

Molecular Rotation Dominated Thermoelasticity. Thermoelasticity underlies the reversible martensitic transitions of materials upon heating and cooling. It involves rapid mechanical reconfiguration resulting from the sudden crystallographic changes of the thermally induced polymorphic transitions. Such thermosalient phenomena[24] in molecular crystals elicit changes not only in the intermolecular packing but also in intramolecular conformations. To illustrate the complex structural transformation in molecular crystals, we construct a coordinate scheme shown in Figure 2A, where $\vec{a}$, $\vec{b}$, and $\vec{c}$ represent the lattice of the primitive cell, and $\vec{u}$, $\vec{v}$, and $\vec{w}$ dictate the molecular orientations. Specifically, the vector $\vec{v}$ aligns with the molecular backbone direction, and $\vec{w}$ connects the molecular mass center with the Si atom in the side group; $\vec{u}$ is determined by the cross product of $\vec{v}$ and $\vec{w}$. ω, φ, and θ are three Euler angles characterizing the rotation of the molecule about the three orientation axes ($\vec{u}$, $\vec{v}$, and $\vec{w}$) with respect to its original orientations. Our prior experiments of differential scanning calorimetry showed two first-order polymorphic transitions of TIPS-pentacene (i.e., Form I/Ib-to-Form II and Form II-to-Form III)[25] associated with the major changes in the lattice parameter b and the angle γ. To examine the underlying molecular mechanism, we adopt an evolutionary genetic algorithm to refine the molecular force field (Materials and Methods), which enables us to model the phase transitions of TIPS-pentacene under various thermal and mechanical

https://dx.doi.org/10.1021/acs.chemmater.1c00080
Chem. Mater. 2021, 33, 1883–1892

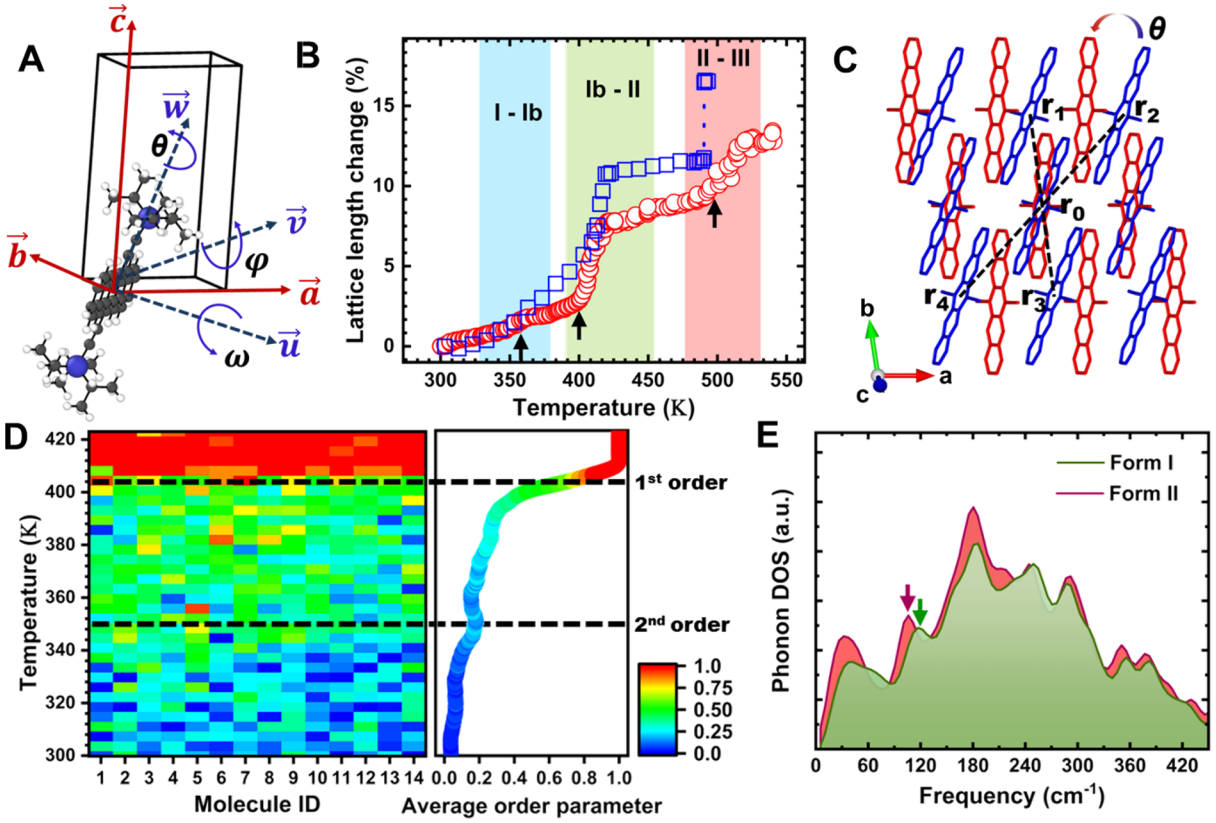

Figure 2. (A) Unit cell of the TIPS-pentacene molecular crystal. (B) Experimental (blue squares) and simulation (red circles) results of the change in the *b*-lattice parameter during heating. (C) Molecular crystal structures of Form I (blue) and Form II (red) show the angular rotation θ of the molecular orientation in the *ab* plane. (D) Contour map of the order parameter of 14 molecules when temperature increases. The average order parameter demonstrates the second-order and first-order phase transitions upon heating. (E) Phonon densities of states show the phonon softening when the structure morphs from Form I (green curve) to Form II (red curve).

loads. Figure 2B shows the experimental (blue squares) and simulation (red circles) results of the change in the *b*-lattice parameter during heating. The discrepancy of ∼2% in experiments and modeling for Forms II and III is not significant considering the limited model size (∼12 nm in *b*) used in the force field training. The abrupt increase of the *b*-lattice parameter at 400 K and 493 K indicates the first-order phase transition of Form I/Ib-to-II and of Form II-to-III, respectively. Furthermore, a second-order transition of Form I-to-Ib is observed with a continuous change of the lattice parameter but a discontinuity in the slope of the lattice parameter at ∼353 K.[25] Since the two first-order transitions are similar, we focus on the phase transition of Form I-to-II within the temperature range 300−423 K. An order parameter is desired to represent individual phases. We determine the order parameter based on the symmetry of the base-centered plane in the monoclinic lattice, consisting of a center molecule and four first nearest neighbor molecules (Figure 2C). The order parameter is defined as $\xi_i = \frac{1}{2}(1 - \cos(\delta_i))$, with $\delta_i = \frac{\pi(\rho_i - \rho_l)}{\rho_h - \rho_l}$ and $\rho_i = (d_2 + d_4) - (d_1 + d_3)$, where d_j refers to the distance between the center molecule (r_0) and each neighbor molecule (r_j), and ρ_l and ρ_h are calculated for the initial and final structures, respectively.

Using the lattice structures obtained from XRD experiments, the ρ values for Forms I, II, and III are approximately 5.0, 2.0, and 0.0, respectively.[23] A smaller value of ρ denotes a more symmetric coordination environment around the center molecule. Therefore, the decreasing value of ρ from Form I to Form III indicates the increase of symmetry during the heating-induced polymorphic transition. The order parameter ξ_i varies from 0 (blue) to 1 (red), corresponding to a polymorphic transition from the parent phase to the daughter phase (e.g., Form I to Form II transition). The lattice deformation is quantified by the deformation gradient matrix *F* transforming the original lattice coordinates ($\vec{a}$, $\vec{b}$, and $\vec{c}$) to the new coordinates ($\vec{a}'$, $\vec{b}'$, and $\vec{c}'$) in the deformed unit cell, which is calculated as $\mathbf{F} = \begin{bmatrix} 0.99 & -0.21 & 0.11 \\ -0.04 & 0.94 & -0.12 \\ 0.02 & 0.03 & 1.04 \end{bmatrix}$. The deformation matrix shows that the lattice cell undergoes a shear deformation of −0.21 in the *ab* plane and a tilt of the *c*-axis in the three-dimensional space. The shear strain results in a reduction of 9.6° in γ between the vectors $\vec{a}$ and $\vec{b}$, which is close to the experimental value of γ changing from 82.2° in Form I to 72.1° in Form II (Table S1). Meanwhile, the change in molecular orientation can be described by the Euler rotational angles. The Euler angles $[\theta, \varphi, \omega]$ are calculated as [9.5°, −1.6°, 2.1°], where the major change of 9.5° in angle θ arises from the counterclockwise molecular rotation about the $\vec{w}$ The result demonstrates that molecular rotation dominates the thermal-induced phase transition from Form I to Form II.

The polymorphic transition of Form I-to-II is accompanied by the homogeneous nucleation and growth of the daughter phase where the nuclei of Form II are randomly distributed within the parent Form I (Figure S1). Here, we plot the evolution of the order parameter for 14 adjacent molecules in a row and the average order parameter of the whole supercell in

https://dx.doi.org/10.1021/acs.chemmater.1c00080
Chem. Mater. 2021, 33, 1883−1892

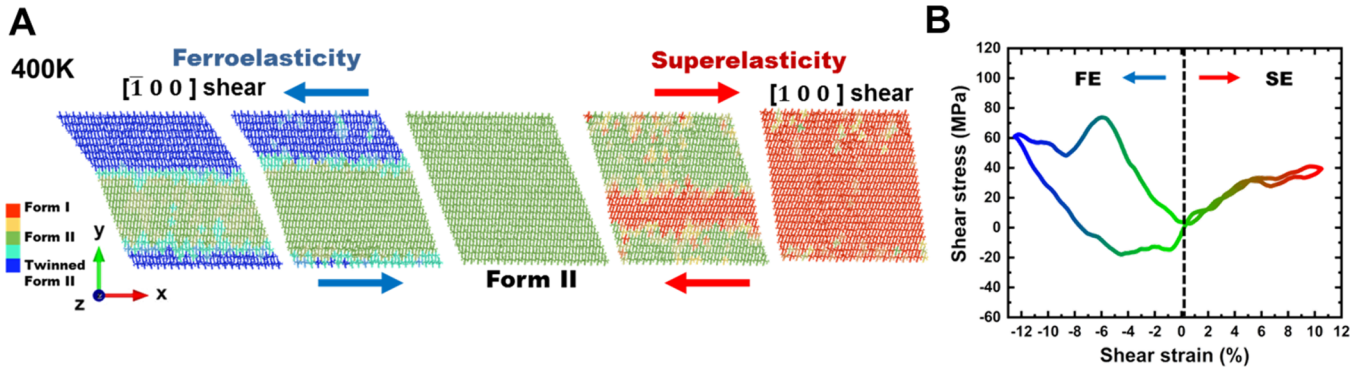

Figure 3. (A) Molecular trajectories of the interconvertible SE and FE of Form II by ⟨1 0 0⟩ shear at 400 K. (B) Their corresponding stress−strain responses. The molecules in part A are color-coded by the order parameter representing the different phases as marked in the color bars.

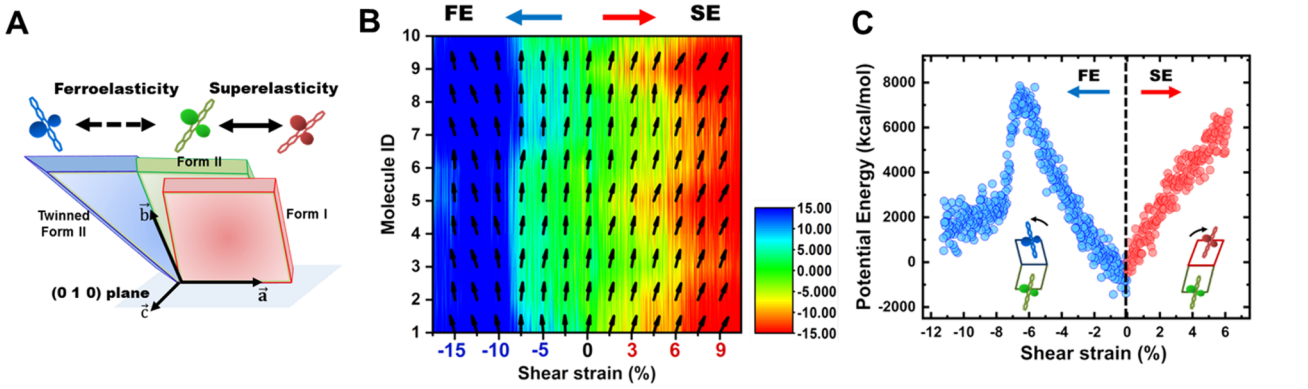

Figure 4. (A) Sketch of the lattice transformation of ferroelasticity and superelasticity in Form II. The cells of different colors represent different polymorphs of distinct molecular orientations. (B) Contour plot of the molecular rotation of 10 molecules in Form II under ⟨1 0 0⟩ shear load. The black arrows are the vectors representing the direction of the molecular orientation. (C) Molecular potential energy as a function of the shear strain when Form II is deformed by shear. The insets show the deformation twinning associated with FE (left) and lattice transition from Form II to Form I associated with SE (right).

Figure 2D. Within the temperature range 300−353 K, most molecules are retained in Form I. Bypassing 353 K, the green domain gradually dominates with a small bump in the average order parameter indicating the second-order phase transition. The abrupt jump of the average order parameter is observed at ∼400 K. A sharp green-to-red transition is observed in the contour map signifying the first-order transition of Form Ib to Form II. We analyze the thermodynamics of the phase transition. At low temperature, Form I is favored by its lower enthalpy and is thermodynamically more stable compared to Form II. When temperature increases, an increase of entropy in Form II is expected to reduce the free energy and triggers the Form I-to-II transition. Since no change of the chemical, electronic, or magnetic states is involved, the entropy change of the diffusionless transformation is mostly vibrational.[26] Figure 2E shows the comparison of the vibrational phonon density of states (PDOS) for Form I and Form II at the frequency region 0−450 cm^{-1}. A clear phonon softening is observed, where the PDOS of Form II is enhanced and shifted to the lower frequency regime. This result is consistent with the Raman spectrum experiment (Figure S2), which identifies the Form I-to-II transition by detecting the peak shift to the lower frequency regime. The phonon softening leads to an increase of 8.7 kcal/mol in the vibrational entropy (Materials and Methods), which is comparable to the value of 10 kcal/mol in our previous calorimetry measurements.[22] PDOS is contributed by both the intra- and intermolecular vibrations. The phonon softening usually correlates with the increase of the collective atomic motions,[27,28] which may be attributed to the symmetry enhancement in the Form I-to-II transition that is promoted by the cooperative rotations of the conjugated backbone and side groups. A similar observation was reported in the martensitic transition of NiTi alloy, where the lower-symmetry B19′ is thermally transformed into the higher-symmetry B2 phase accompanied by the phonon softening and entropy increase.[29]

Interconvertible Behavior of Superelasticity and Ferroelasticity. Superelasticity is generally achieved by a reversible martensitic transition. The austenitic (mother) phase spontaneously reforms when the external load is released. As a comparison, ferroelasticity is often accomplished by deformation twinning, and the structure recovers its original shape when loaded in an opposite direction. Figure 3 shows the snapshots of the molecular structure in the ferroelasticity and superelasticity of TIPS-pentacene at 400 K. The molecules of different phases are color-coded by the order parameter. This demonstrates that SE and FE are interconvertible in Form II under ⟨1 0 0⟩ shear. The interconvertibility represents the shear deformation along [$\bar{1}$ 0 0] transforming Form II to a twinned phase, while the opposite load along [1 0 0] recovers Form II to the original shape, and a further increase of the shear strain leads to the superelasticity and a self-recoverable transition of Form II-to-I. Figure 3B plots the corresponding stress−strain responses. A large hysteresis loop in the shear

https://dx.doi.org/10.1021/acs.chemmater.1c00080
Chem. Mater. 2021, 33, 1883−1892

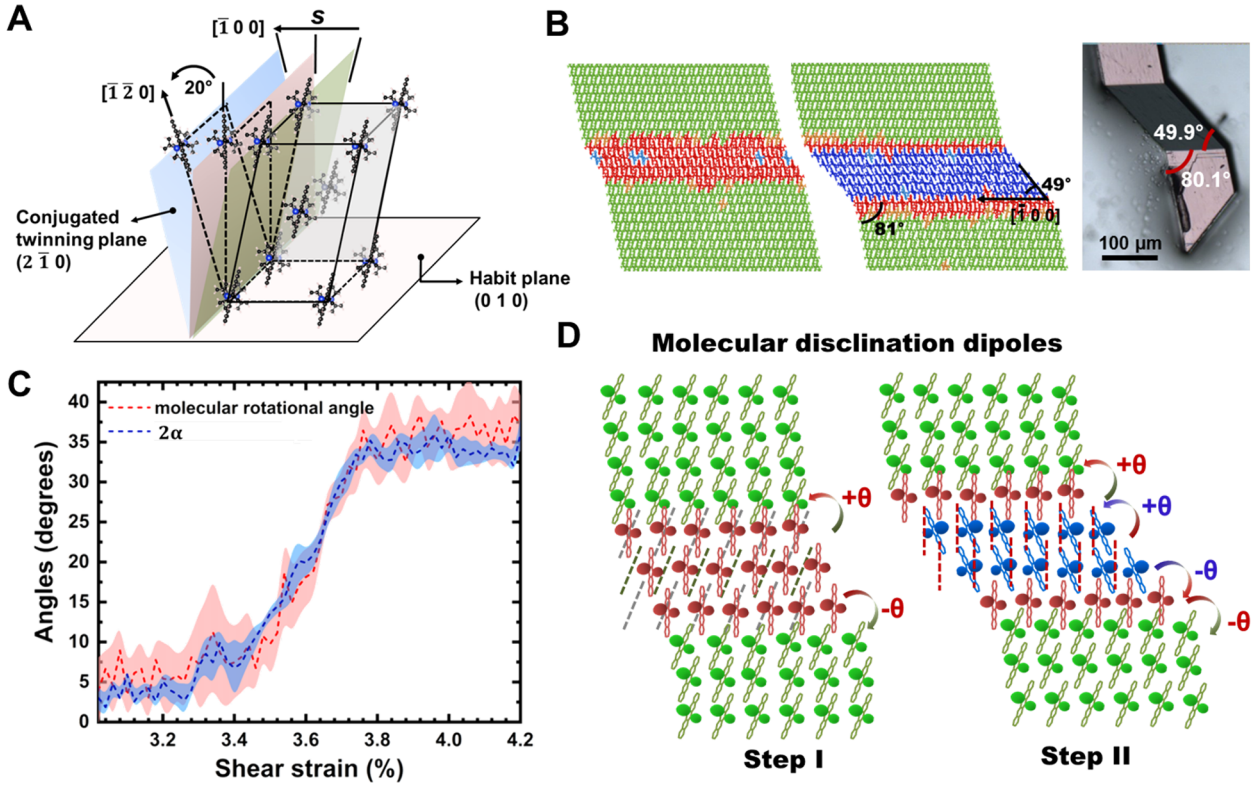

Figure 5. (A) Illustration of the twinning elements of FE-I in Form II. (B) Snapshots of the molecular structure showing the metastable phase (red) and the twinned phase (blue). The twinning angles in the modeling match well with the experimental observation (optical image). (C) Correlation between the molecular rotational angle (red) and the angle (2α) between the conjugated twinning planes (blue). The dotted curves denote the mean values for five different cells in the modeling, and the shaded areas represent the standard deviations. (D) Two-step twinning formation achieved by molecular disclination dipoles.

cycle is shown in the ferroelastic process, while superelasticity proceeds with a much smaller stress hysteresis.

Figure 4A illustrates the lattice transformation of ferroelasticity and superelasticity in Form II. The cells of different colors represent different polymorphs of distinct molecular orientations. Although SE and FE involve distinct lattice changes and molecular motions, they share the same (0 1 0) habit plane, which provides the crystallographic basis for the interconvertible behavior. Lattice transformation in SE and FE can be described by the deformation gradient matrix and the Euler rotational angles. For FE, the lattice deformation matrix is $\mathbf{F} = \begin{bmatrix} 1.03 & -0.28 & 0 \\ 0.06 & 1.06 & 0 \\ -0.01 & 0 & 1 \end{bmatrix}$, which shows a simple shear deformation with a shear component of −0.28 in the *ab* plane. The Euler angles $[\theta, \varphi, \omega]$ are $[11°, -3°, 0.57°]$, where the major orientational change is the counterclockwise rotation in θ about the $\vec{w}$-axis. In SE, where the Form II-to-I phase transition occurs, the Bain strain matrix[15] is calculated as $\mathbf{B} = \begin{bmatrix} 0.99 & 0.20 & 0 \\ -0.03 & 0.89 & 0 \\ 0.02 & 0 & 1 \end{bmatrix}$, which shows a simple shear component of 0.20 and a compression of 0.11 along the *b*-axis upon the transition. The associated Euler angles are $[-9.8°, 8.9°, 1.8°]$. The clockwise rotation of 9.8° in θ denotes the shear deformation. Meanwhile, a notable change of 8.9° in φ occurs as molecules rotate counterclockwise about the $\vec{v}$-axis, which is related to the shrinkage in the *b*-lattice parameter. It is worth noting that the characteristic shear strain in the Bain matrix and the θ angle in the Form II-to I superelastic transition are opposite to those of Form I-to-II thermoelastic transition, showing the equivalence of thermal and mechanical load on modulating the polymorphic transitions.[30]

The concerted molecular rotation is a striking characteristic of SE and FE in the organic crystal. Figure 4B shows a contour map of the molecular rotation for 10 molecules in a row under ⟨1 0 0⟩ shear deformation. The color scheme represents the change in angle θ with respect to its original value. The black arrow denotes the positive $\vec{v}$ vector of each molecule, which aligns with the direction of the molecular backbone. All molecules in the supercell of Form II are subjected to a shear strain with the magnitude varying from −17.5% to +11.5%. During the shear deformation, the molecular orientation is collectively adapted to the shear direction. Such rotational adapting behavior is perhaps analogous to the process where a magnetic/electric dipole ($\vec{p}$) seeks to align with the applied magnetic/electric field ($\vec{B}$) in favor of the energy reduction $E = -\vec{p}\cdot\vec{B}$.[31] Intuitively, we may regard each molecule as an independent and rigid "compass needle" exposed to the stress field. Compared to the [1 0 0] shear-induced superelastic transition, ferroelastic twinning is expected to carry a larger energy reduction of the system because the molecules need to rotate by a bigger angle to align with the $[\bar{1}\ 0\ 0]$ shear (see the sketch in Figure 4A). In FE, a sharp transition front of the molecular orientation is observed at −7.5% shear strain, where the molecules flip the orientation concurrently so that the projection of the molecular orientation becomes parallel to the shear direction. Such concerted rotational motion is absent when the molecules are subject to [1 0 0] shear in SE, where a diffusive transition front at ∼5% strain is observed in the contour map. The asynchronous molecular orientations in the

https://dx.doi.org/10.1021/acs.chemmater.1c00080
Chem. Mater. 2021, 33, 1883−1892

(0 1 0) layer are also evident in both the experiments and molecular trajectories of SE (Figure 3A). The structural responses of SE and FE are related to their difference in the potential energy profile (Figure 4C). The potential energy of ferroelastic deformation increases linearly in the early elastic response to the shear deformation and then quickly drops after the barrier of the concerted drastic rotation of molecules is passed. In comparison, the potential energy of SE continuously increases with a slight drop when the transition occurs at ~4.5% shear strain, when the molecules orientate along the shear direction. Overall, the superelastic transition is absent of the dissipation mechanism of the free energy, and the stored mechanical energy facilitates shape recovery upon removal of the shear load. Deformation twinning is the carrier of the substantial energy loss in FE. The molecules restore the initial shape through detwinning under a reverse load. The inset in Figure 4C sketches the lattice changes in FE and SE, with the upper cell showing the transformed phase and the lower one the original Form II. From the lattice transformation matrix, we learn that the simple shear deformation in FE renders the original and transformed lattices packed with a mirror symmetry, which minimizes the interfacial energy and stabilizes the phase boundary. In contrast, the compression in the *b*-axis shown in the Bain strain matrix for SE dictates a considerable strain energy at the Form II−I interface, which in turn contributes to the spontaneous shape recovery upon unloading.

The interconvertible SE and FE demonstrate the rich polymorphic changes in TIPS-pentacene adaptive to the external load. Such interchangeability is absent in shape memory alloys because the transitions in atomic compounds only involve displacive motions of atoms. The indistinguishable atomic orientation at each lattice site in metallic alloys cannot render the distinct transitions on the same habit planes. The molecular packing enhances the mechanical versatility of organic systems. Mechanical deformation can be potentially utilized during and/or after solution processing to manipulate the molecular structure and used as an effective way to investigate their structure−property relationships in various polymorphs.[21,32]

Molecular Twinning. We make a closer examination on the nucleation and crystallographic principle of molecular twinning in the ferroelasticity of TIPS-pentacene. We described two types of ferroelasticity mediated by deformation twinning in Figure S3—FE-I by $[\bar{1}\ 0\ 0]$ shear and FE-II by [0 1 0] tension at 300 K. In the two ferroelastic transitions, Form I first transforms to an intermediate metastable phase and then forms the twinned phase. We determine the molecular kinetics of the two forms of ferroelasticity separately. Phenomenological theories[15,33] are also used here to describe the crystallography of twinning in molecular crystals. In FE-I, the base centered lattice shown in Figure 5A is used to present the molecular trajectories, where one molecule resides at each corner, and two molecules occupy the center of the front and back planes, respectively. The crystallographic relationships between the parent and twinned lattices can be described by four independent twinning elements (K_1, K_2, η_1, η_2).[16,34] In FE-I, K_1 is the undistorted and unrotated habit plane (0 1 0). K_2 is the conjugated twinning plane which is undistorted but rotated. This plane is marked as K_2^T in the twinned lattice. K_2/K_2^T is the $(2\ \bar{1}\ 0)$ plane in FE-I. The molecules in the K_2 plane point to the $[\bar{1}\ \bar{2}\ 0]$ direction, which is defined as the η_2/η_2^T conjugated twinning direction. η_1 denotes the shear direction $[\bar{1}\ 0\ 0]$. Along the η_1 direction, twinning proceeds with a shear amount of $S = 2\tan(\alpha)$, where the angle α represents half of the angle between η_2 and η_2^T. Upon deformation twinning, the molecular backbone along the η_2 direction ($\vec{v}$-axis in Figure 2A) rotates in the counterclockwise direction. With the given initial molecular crystallography of Form I, α can be theoretically determined as 20°. The twinning elements (K_1, K_2, η_1, η_2) fully describe the deformation gradient matrix in the following form:[16]

$$\mathbf{S} = \begin{bmatrix} 1 + sm_1n_1 & sm_1n_2 & sm_1n_3 \\ sm_2n_1 & 1 + sm_2n_2 & sm_2n_3 \\ sm_3n_1 & sm_3n_2 & 1 + sm_3n_3 \end{bmatrix}$$

where $\vec{m}$ represents the twinning direction, and $\vec{n}$ is the normal vector of the K_1 plane. In FE-I, the shear amount is given by $s = 2\tan(20°) = 0.73$. $\vec{m}$ and $\vec{n}$ are $[\bar{1}\ 0\ 0]$ and [0 1 0], respectively. These values determine the deformation matrix as $\begin{bmatrix} 1 & -0.73 & 0 \\ 0 & 1 & 0 \\ 0 & 0 & 1 \end{bmatrix}$. In the simulation, the deformation matrix is calculated as $\begin{bmatrix} 1.01 & -0.74 & 0 \\ -0.04 & 1.07 & 0 \\ -0.02 & -0.01 & 1 \end{bmatrix}$, which agrees well with the theoretical prediction. The Euler angles $[\theta, \varphi, \omega]$ are further determined as [42.7°, −4.2°, −4.0°], which shows the characteristic rotational change of 42.7° in θ in the FE-I transformation.

The molecular structures of the intermediate metastable and twinned phases are shown in the snapshots of Figure 5B. Upon $[\bar{1}\ 0\ 0]$ shear, the molecular backbones rotate counterclockwise by 20°, generating a metastable phase with the molecular packing close to Form III. A further counterclockwise rotation of 20° leads to the final phase with a mirror symmetry of the pristine polymorph. The twinning angles in the modeling match well with the experimental results as shown in the optical imaging. Figure 5C illustrates the correlation between the molecular rotational angle and the angle between the conjugated twin planes 2α. The dotted lines denote the mean values for five different cells, each containing five molecules, at different locations of the entire simulation model in order to minimize the statistical variation. The shaded areas represent the standard deviations. The molecular structural features demonstrate that deformation twinning in ferroelastic transformation is dominated by the overall molecular rotation. The orientational motion at the twinning interface is close to the concept of a disclination, which is an extended structure originally proposed by Volterra[35] and has been used to describe the linear rotational defect in the reorientation of molecules in liquid crystals.[36] Under external (thermal, mechanical, electrical) stimuli, a rapid change in the preferred orientation in the vicinity of a line/point is recognized as disclination.[37] Molecules in TIPS-pentacene in the (0 1 0) plane have sufficient flexibility to adapt their orientations to the external shear as shown in Figure 4B, which behave similarly with the loosely packed molecules in liquid crystal. By this analogy, we define the orientational perturbation in the twinning process of FE-I as the molecular disclination dipole, as shown in Figure 5D. Here, individual layers show molecular rotations, rather than translations, and thus are indicative of disclination rather than dislocation movement. In the intermediate phase, a counterclockwise rotation of $+\theta$ (20°) in the upper transformed layer (red molecules) is required

https://dx.doi.org/10.1021/acs.chemmater.1c00080
Chem. Mater. 2021, 33, 1883−1892

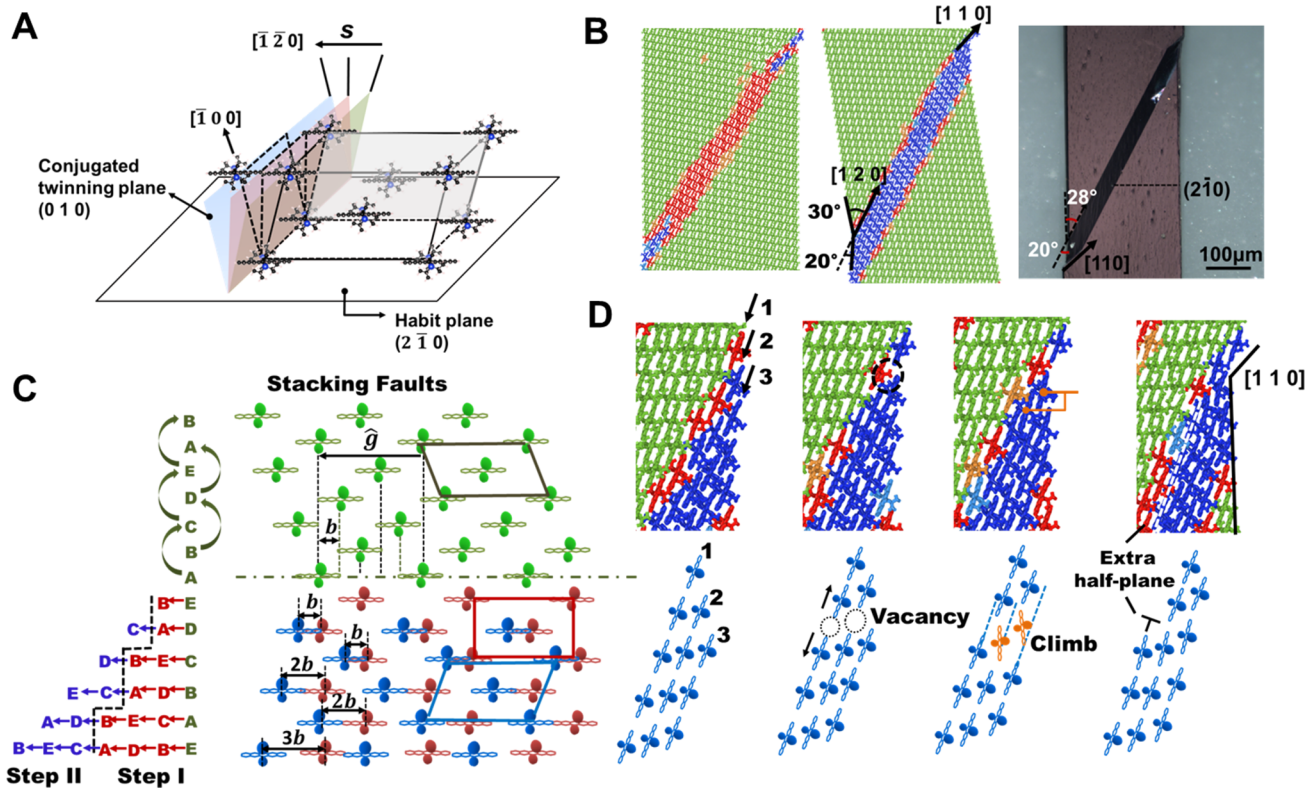

Figure 6. (A) Twinning elements of FE-II in Form II. (B) Snapshots of the molecular structure upon mechanical load showing the metastable phase (red) and the twinned phase (blue). The optical image shows the crystallography of twinning and a surface crack in experiments. (C) Two-step formation mechanism of twinning by the stacking faults. (D) Snapshots (upper panel) demonstrate the ejection of a molecular dislocation accompanying the twinning process. The lower panel shows the magnified view of vacancy formation and dislocation climb in the (2 $\bar{1}$ 0) layers.

while a clockwise operation of $-\theta$ can recover the initial state at the lower bound. Such paired rotational operations are defined as molecular disclination dipoles. The metastable phase proceeds by an additional pair of $\pm\theta$ rotational operations and forms the twinned phase (blue molecules). Compared with the continuous variation in molecular orientation in liquid crystals, the disclination dipoles in TIPS-pentacene have well-determined, quantized rotational operations and therefore retain their molecular order. The shearing operation of twinning and martensitic transformation in metals[15,16] is considered to be carried out through coordinated dislocation movement, which translates each (or every other) layer of the crystal individually. The rotational operation of an individual molecular layer does not accumulate with dipoles as it would with individual disclinations and is carried on sequentially by the successive layers, which eliminates potential molecular packing faults. Hence, the unique molecular disclination dipoles promise a strong structural integrity in FE-I. The molecular packing in both the experiments and simulations is well retained without structural disruption.

Following the same procedure, we analyze the crystallographic principle of twinning in FE-II. As sketched in Figure 6A, the base centered lattice cell is subject to a [$\bar{1}$ $\bar{2}$ 0] shear with a habit plane of (2 $\bar{1}$ 0). The conjugated twinning plane and conjugated twinning direction are (0 1 0) and [$\bar{1}$ 0 0], respectively. It is interesting to note that the twinning elements of FE-II are essentially the reciprocal of those of FE-I: $K_1^{\text{FE-II}} = K_2^{\text{FE-I}}$, $K_2^{\text{FE-II}} = K_1^{\text{FE-I}}$, $\eta_1^{\text{FE-II}} = \eta_2^{\text{FE-I}}$, and $\eta_2^{\text{FE-II}} = \eta_1^{\text{FE-I}}$.[15] The twinning in FE-II is mainly driven by the [$\bar{1}$ $\bar{2}$ 0] shear component of the applied tension in [0 1 0], while other stress components cause tilt of the lattice. In the phenomenological theory, deformation twinning in FE-II is described by keeping its interface plane unrotated during the transition. The twinning elements to construct the deformation gradient matrix are $s = 2\tan(20°) = 0.73$, $\vec{m} = [\bar{1}\ \bar{2}\ 0]$, and $\vec{n} = [2\ \bar{1}\ 0]$, which yields the deformation gradient matrix $\begin{bmatrix} 0.64 & 0.18 & 0 \\ -0.73 & 1.36 & 0 \\ 0 & 0 & 1 \end{bmatrix}$. The theoretical prediction is again close to the lattice deformation matrix in the simulation $\begin{bmatrix} 0.69 & 0.18 & -0.01 \\ -0.64 & 1.21 & 0.08 \\ -0.04 & 0.02 & 1.01 \end{bmatrix}$. Given that the molecular backbones are coaligned on the (2 $\bar{1}$ 0) habit plane (Figure 6A), and the shear direction [$\bar{1}$ $\bar{2}$ 0] aligns with the backbone orientation, the deformation twinning in FE-II is accommodated by the displacive motion of the molecules rather than the rotational disclination as described in FE-I. The twinning kinetics also consists of two steps, where a metastable phase first emerges along the habit plane before the formation of the twinned phase (Figure 6B). The twinned molecular structure in the simulation agrees well with the optical observation in the experiments. We also note that surface cracks along the [1 1 0] direction in the twinning configuration are often observed in the FE-II experiments, which largely compromise the electronic performance of the stretchable semiconductor device over cycles. The formation mechanism of twinning and cracking is understood by the stacking faulting and molecular dislocations. Figure 6C demonstrates the stacking sequence of *ABCDE* along the [2 $\bar{1}$ 0] direction of TIPS-pentacene. Due to the two-dimensional brickwork packing molecular structure, the *ABCDE* stacking

https://dx.doi.org/10.1021/acs.chemmater.1c00080
Chem. Mater. 2021, 33, 1883−1892

follows an alternative transformation sequence, that is, $A \rightarrow C \rightarrow E \rightarrow B \rightarrow D \rightarrow A$, upon the displacive motion. A stacking fault can be formed by the molecular partial dislocation $\vec{b} = \frac{1}{5}\hat{g}$, where $\hat{g}$ denotes the vector connecting the two adjacent molecules on the $(2\ \bar{1}\ 0)$ habit plane (Figure 6C). Figure 6C illustrates the details of the two-step mechanism of the twinned Form I based on the stacking faults. First, a metastable phase is produced by the motion of the partial dislocations on "odd number" alternate layers, where the original stacking sequence of *EDCBAE* is transformed locally into the sequence *BABABA*. Then, the twin embryo is generated by a further motion of partial dislocations on the "even number" alternate layers, resulting in the final stacking sequence of *BCDEAB*. Such a two-step formation process of molecular twinning in TIPS-pentacene is analogous to the FCC/HCP twinning mechanism where, in the FCC lattice, Shockley partial dislocations transform the stacking of *ABCABC* in FCC to an intermediate stacking of *ABABAB* (HCP) and eventually to the stacking of *ACBACB* as twinned FCC.[38] The stacking faulting correlates with the phenomenological theory (Figure 6A). Half of the twinning shear amount is essentially the ratio of the length of the burgers vector $\vec{b}$ to the spacing of the $\{2\ \bar{1}\ 0\}$ plane. This sequential stacking transition guarantees the undistorted conjugated twinning plane K_2^T in the twinned phase. In the twinning transition, the glide motion of $(2\ \bar{1}\ 0)$ molecules may result in the ejection of a full dislocation. The upper panel in Figure 6D depicts four representative molecular trajectories in this process. For ease of view, we show the details of three $(2\ \bar{1}\ 0)$ molecular layers of interest in the lower panel. The three layers are initially packed as twinned Form I (first snapshot). Two vacancies are generated by the asynchronous gliding of the neighboring molecules within one molecular layer (second snapshot), possibly due to the inhomogeneity of the strain field near the surface or thermal fluctuation. Then, two adjacent molecules (orange in the third snapshot) tilt their backbone orientation toward the center of the vacancies in response to the attractive forces from the dangling intermolecular "bonds" around the vacancies. The newly formed intermolecular bonds migrate the molecules originally in layers 1 and 2 to the layers 2 and 3, respectively, which results in the climb of the vacancies across the $(2\ \bar{1}\ 0)$ habit plane (fourth snapshot). After equilibrium, an extra half-plane is formed in the model with the appearance of a step crack along the $[1\ 1\ 0]$ direction that verifies the experimental observation. Both the formation and climb of vacancies involve the cooperative motion of a molecule pair, which may arise from the pair attraction between two adjacent backbones as well as the steric hindrance effect of the side groups of two nearest molecules. To prevent crack formation due to the asynchronous molecular glide, a slight increase in temperature may eliminate the precursor of the vacancies, or a design of less bulky side groups may help reduce the glide resistance from the neighboring molecules.

CONCLUSIONS

We systematically study the thermodynamics and evolution of the lattice structure, molecular conformation, and interfacial kinetics of the versatile cooperative transitions in TIPS-pentacene molecular crystals. The quantitative agreement between molecular modeling, theoretical analysis, and experiments demonstrates that the three-dimensional molecular rotations dictate the lattice transformation in the thermo-, super-, and ferroelastic transitions. The interconvertible behavior of super- and ferroelastic transitions represents the distinct directional responses of the molecular crystal under $\langle 1\ 0\ 0\rangle$ shear loading. We elucidate for the first time the molecular defects of disclination dipoles and molecular stacking faults associated with molecular twinning. The mechanistic understanding sheds insight on devising the cooperative transitions in a variety of organic solids for a new avenue of environmentally responsive organic electronics through molecular design.

MATERIALS AND METHODS

Molecular Dynamics. The simulation is carried out using the molecular dynamics software LAMMPS package.[39] The OPLS-AA force field[40] is adopted to describe the molecular interactions. The supercell of Form I is built by expanding the unit cell obtained from the XRD experiments, containing 51 200 atoms (512 molecules) with a size of 12.8 nm × 12.3 nm × 3.3 nm (along the *X*, *Y*, and *Z* directions). The structure is energetically relaxed under NPT at 300 K and zero pressure for 0.5 ns. Heating is conducted in the range 300−550 K with a heating rate of 0.625 K/ps. The generated Form II supercell at 400 K is subject to $\langle 1\ 0\ 0\rangle$ shear to induce the SE and FE-I. At 300 K, FE-I and FE-II are induced by applying $[\bar{1}\ 0\ 0]$ shear and $[0\ 1\ 0]$ tension on the supercell (12.8 nm × 30.8 nm × 3.3 nm) of Form I, respectively. The $[0\ 1\ 0]$ tension is performed by applying a tensile load along the *y*-axis in the Cartesian coordinate to preserve a constant loading direction and rate. The shear strain with an engineering strain rate of 0.02%/ps is applied under NVT. The tensile load is applied under NPT with a strain rate of 0.02%/ps, while the supercell size in other dimensions is allowed to shrink. Unloading is conducted by applying the reverse shear/tensile strain until the resultant strain is reduced to zero. The resolved stress/strain relationship along the shear direction $[1\ 2\ 0]$ is calculated in FE-II.[41] Periodic boundary conditions are prescribed in all directions. Temperature and pressure are controlled using the Nosé−Hoover thermostat and barostat with a time step of 0.1 fs.

Genetic Algorithm Training. In the OPLS-AA force field, the energetic parameters for intramolecular interactions (bond, angle, torsional, improper) were carefully calibrated in our previous work.[23] This study focuses on the parametric training of the intermolecular potential including the Coulombic and van der Waals interactions (Figure S4A,B), which is crucial for simulating the structural changes in organic solids. Since the electrostatic potential usually acts more strongly than van der Waals interactions,[42] we first calibrate the Coulombic partial charges to obtain Form II at 400 K. Next, van der Waals parameters are refined to capture the phase evolution. Then, Form II-to-III transition is examined at 500 K to determine whether the training succeeds. To perform the optimization in a space of high dimensionality, we adopt the genetic algorithm, which is an evolutionary algorithm that mimics the natural selection process. In Coulombic parametric training, we start with the seed parameters obtained by the electrostatic potential (ESP) fitting and generate the first generation by randomly populating a set of parameters that lie within the physically allowable limit (±1.5 times) of the seed while retaining the charge neutrality. The objective function is defined as $F_1 = \frac{1}{2}\sqrt{\left(\frac{b'-b}{b}\right)^2 + \left(\frac{\gamma'-\gamma}{\gamma}\right)^2}$, where the lattice length b and angle γ are the experimental values for Form II, and b' and γ' denote the simulated values. The sets of parameters are then ranked in ascending order of the evaluation values of the objective function. 60% of parameters with the lowest values are selected to perform the genetic operations of mutation with a rate of 5% and crossover with a rate of 10%. The optimization succeeds if the objective function converges (<5%). Any failure in convergence will lead to the next offspring generation. At this stage, van der Waals parameters from the OPLS database are preserved, and a cutoff distance of 8 Å is chosen for all intermolecular interactions. 105 sets of best partial charges selected from 50 generations (100 populations for each generation) are further

https://dx.doi.org/10.1021/acs.chemmater.1c00080
Chem. Mater. 2021, 33, 1883−1892

examined by the screening criteria of $\frac{1}{4}\sqrt{\sum\left(\frac{p_i' - p_i}{p_i}\right)^2} < 10\%$, where p_i' and p_i refer to the simulated and experimental values for other lattice parameters except for b and γ. Next, in the training of the van der Waals parameter, to capture the characteristics of the first-order transition, a fine criterion is chosen as $F_{II} = \frac{|(\varepsilon_h - \varepsilon_l) - \delta|}{\delta}$, where ε_l and ε_h are the low and high bound values of b length change at the transition point, and δ denotes the change measured by experiments. Lastly, the cutoff radii for the two potentials are slightly tuned within ±1.2 times of 8 Å to achieve the best fitting performance. The trained intermolecular parameters are listed in Tables S2 and S3. The simulated lattice parameters of three polymorphs and the percentage change of lattice length b match well with experiments (Table S1, and Figure 2B).

Lattice Dynamics. The velocity autocorrelation function (VACF) method[43] is used to calculate PDOS. The supercells of Form I and Form II are first relaxed under NVT at 300 K, and then, their VACFs are calculated and spatially averaged over a 2 ps period under NVE 10 times.

$$\mathrm{VACF}(t) = \frac{\langle v(t)\cdot v(0)\rangle}{\langle v(0)^2\rangle}$$

PDOS $g(w)$ is obtained by performing the Fourier transformation onto VACF with a frequency interval of 5 cm^{-1}. By taking each atom as a harmonic oscillator, the vibrational entropy is calculated as

$$S_{vib} = -k_B\int_0^\infty g(\omega)\ln\left[1 - \exp\left(\frac{h\omega}{k_BT}\right)\right]d\omega + k_B\int_0^\infty g(\omega)\frac{\frac{h\omega}{k_BT}}{\exp\left(\frac{h\omega}{k_BT}\right) - 1}d\omega$$

Raman Spectroscopy. Variable-temperature Raman spectra of TIPS-P are obtained using a Horiba Raman confocal imaging microscope (LabRAM HR 3D) with an 832 nm laser excitation source. The spectra are obtained using a 50× long working distance objective lens, a 300 mm^{-1} grating, and an optical density filter of OD = 0.03. Temperature is controlled using a Linkam THMS600 stage.

Single-Crystal Crystallography and Optical Microscopy. Single crystals of TIPS-pentacene were obtained either by drop-casting decane solution (8 mg mL^{-1}) onto octadecyltrichlorosilane-treated silicon substrate or by recrystallization in ethyl acetate. The single-crystal structures of Form I and II polymorphs were solved based on diffraction patterns collected using a Bruker D8 Venture instrument.[22] In the case of Form III, diffraction patterns were collected at NSF's ChemMatCARS (sector 15) of the Advanced Photon Source, Argonne National Laboratory.[23] Deposition numbers CCDC 1570910 (Form I), 1570911 (Form II), and 1991343 (Form III) contain the supplementary crystallographic data for this paper. The change in b-lattice parameter (Figure 2B) is evaluated by measuring the elongation of the crystal sample along the long-axis (b-axis) during heating. Optical micrographs of twinned crystals are obtained using a Nikon Eclipse Ci-POL optical microscope equipped with a high-speed camera (Infinity 1, Lumenera Corp.).

■ ASSOCIATED CONTENT

Supporting Information

The Supporting Information is available free of charge at https://pubs.acs.org/doi/10.1021/acs.chemmater.1c00080.

Molecular trajectories of phase transitions upon heating and mechanical loads, Raman spectrum of three polymorphs, flowchart of genetic-algorithm refined parametric training, comparison of simulated lattice parameters and experimental data, and nonbonded force field parameters (PDF)

■ AUTHOR INFORMATION

Corresponding Authors

Eric P. Kvam − *School of Materials Engineering, Purdue University, West Lafayette, Indiana 47907, United States*; Email: kvam@purdue.edu

Kejie Zhao − *School of Mechanical Engineering, Purdue University, West Lafayette, Indiana 47907, United States*; orcid.org/0000-0001-5030-7412; Email: kjzhao@purdue.edu

Authors

Hong Sun − *School of Mechanical Engineering, Purdue University, West Lafayette, Indiana 47907, United States*; orcid.org/0000-0002-3586-7400

Sang Kyu Park − *Department of Chemical and Biomolecular Engineering, University of Illinois Urbana−Champaign, Urbana, Illinois 61801, United States*

Ying Diao − *Department of Chemical and Biomolecular Engineering, University of Illinois Urbana−Champaign, Urbana, Illinois 61801, United States*; orcid.org/0000-0002-8984-0051

Complete contact information is available at: https://pubs.acs.org/10.1021/acs.chemmater.1c00080

Author Contributions

K.Z., Y.D., and E.P.K. conceived the idea and supervised the study. H.S. performed the molecular modeling and analysis. S.K.P. conducted experimental validation. All authors contributed to writing the paper.

Notes

The authors declare no competing financial interest.

■ ACKNOWLEDGMENTS

H.S. and K.Z. are grateful for the support from the National Science Foundation through grant CMMI-1941323. S.K.P. and Y.D. acknowledge the Alfred P. Sloan Foundation for the Sloan Research Fellowship in Chemistry and 3M Nontenured Faculty Award that supported this work. Single-crystal X-ray diffraction was in part carried out at the ChemMatCARS Sector of Advanced Photon Source, Argonne National Lab, supported by the National Science Foundation under grant NSF/CHE-1834750.

■ REFERENCES

(1) Ghosh, S.; Reddy, C. M. Elastic and bendable caffeine cocrystals: implications for the design of flexible organic materials. *Angew. Chem., Int. Ed.* **2012**, *51*, 10319−10323.

(2) Worthy, A.; Grosjean, A.; Pfrunder, M. C.; Xu, Y.; Yan, C.; Edwards, G.; Clegg, J. K.; McMurtrie, J. C. Atomic resolution of structural changes in elastic crystals of copper (II) acetylacetonate. *Nat. Chem.* **2018**, *10*, 65−69.

(3) Panda, M. K.; Ghosh, S.; Yasuda, N.; Moriwaki, T.; Mukherjee, G. D.; Reddy, C. M.; Naumov, P. Spatially resolved analysis of short-range structure perturbations in a plastically bent molecular crystal. *Nat. Chem.* **2015**, *7*, 65−72.

(4) Ahmed, E.; Karothu, D. P.; Warren, M.; Naumov, P. Shape-memory effects in molecular crystals. *Nat. Commun.* **2019**, *10*, 1−9.

(5) Liu, H.; Lu, Z.; Tang, B.; Qu, C.; Zhang, Z.; Zhang, H. A Flexible Organic Single Crystal with Plastic-Twisting and Elastic-Bending Capabilities and Polarization-Rotation Function. *Angew. Chem., Int. Ed.* **2020**, *59*, 12944.

(6) Naumov, P.; Karothu, D. P.; Ahmed, E.; Catalano, L.; Commins, P.; Mahmoud Halabi, J.; Al-Handawi, M. B.; Li, L. The Rise of the Dynamic Crystals. *J. Am. Chem. Soc.* **2020**, *142*, 13256−13272.

(7) Saha, S.; Mishra, M. K.; Reddy, C. M.; Desiraju, G. R. From molecules to interactions to crystal engineering: mechanical properties of organic solids. *Acc. Chem. Res.* **2018**, *51*, 2957−2967.
(8) Ahmed, E.; Karothu, D. P.; Naumov, P. Crystal adaptronics: mechanically reconfigurable elastic and superelastic molecular crystals. *Angew. Chem., Int. Ed.* **2018**, *57*, 8837−8846.
(9) Zeng, H.; Wasylczyk, P.; Parmeggiani, C.; Martella, D.; Burresi, M.; Wiersma, D. S. Light-fueled microscopic walkers. *Adv. Mater.* **2015**, *27*, 3883−3887.
(10) Kim, T.; Zhu, L.; Al-Kaysi, R. O.; Bardeen, C. J. Organic photomechanical materials. *ChemPhysChem* **2014**, *15*, 400−414.
(11) Koshima, H.; Matsuo, R.; Matsudomi, M.; Uemura, Y.; Shiro, M. Light-driven bending crystals of salicylidenephenylethylamines in enantiomeric and racemate forms. *Cryst. Growth Des.* **2013**, *13*, 4330−4337.
(12) Takamizawa, S.; Miyamoto, Y. Superelastic organic crystals. *Angew. Chem.* **2014**, *126*, 7090−7093.
(13) Engel, E. R.; Takasaki, Y.; Mir, S. H.; Takamizawa, S. Twinning ferroelasticity facilitated by the partial flipping of phenyl rings in single crystals of 4, 4′-dicarboxydiphenyl ether. *R. Soc. Open Sci.* **2018**, *5*, 171146.
(14) Tadaki, T.; Otsuka, K.; Shimizu, K. Shape memory alloys. *Annu. Rev. Mater. Sci.* **1988**, *18*, 25−45.
(15) Christian, J. W. *The theory of transformations in metals and alloys: Part I*; Pergamon Press: Oxford, 1975.
(16) Bilby, B. A.; Crocker, A. The theory of the crystallography of deformation twinning. *P. R. Soc. A-Math. Phys.* **1965**, *288*, 240−255.
(17) van den Ende, J. A.; Ensing, B.; Cuppen, H. M. Energy barriers and mechanisms in solid-solid polymorphic transitions exhibiting cooperative motion. *CrystEngComm* **2016**, *18*, 4420−4430.
(18) Sasaki, T.; Sakamoto, S.; Takasaki, Y.; Takamizawa, S. A Multidirectional Superelastic Organic Crystal by Versatile Ferroelastical Manipulation. *Angew. Chem., Int. Ed.* **2020**, *59*, 4340−4343.
(19) Sasaki, T.; Sakamoto, S.; Takamizawa, S. Twinning organosuperelasticity of a fluorinated cyclophane single crystal. *Cryst. Growth Des.* **2019**, *19*, 5491−5493.
(20) Mei, J.; Diao, Y.; Appleton, A. L.; Fang, L.; Bao, Z. Integrated materials design of organic semiconductors for field-effect transistors. *J. Am. Chem. Soc.* **2013**, *135*, 6724−6746.
(21) Diao, Y.; Tee, B. C.; Giri, G.; Xu, J.; Kim, D. H.; Becerril, H. A.; Stoltenberg, R. M.; Lee, T. H.; Xue, G.; Mannsfeld, S. C. Solution coating of large-area organic semiconductor thin films with aligned single-crystalline domains. *Nat. Mater.* **2013**, *12*, 665−671.
(22) Chung, H.; Dudenko, D.; Zhang, F.; D'Avino, G.; Ruzie, C.; Richard, A.; Schweicher, G.; Cornil, J.; Beljonne, D.; Geerts, Y.; Diao, Y. Rotator side chains trigger cooperative transition for shape and function memory effect in organic semiconductors. *Nat. Commun.* **2018**, *9*, 278.
(23) Park, S. K.; Sun, H.; Chung, H.; Patel, B. B.; Zhang, F.; Davies, D. W.; Woods, T. J.; Zhao, K.; Diao, Y. Super-and Ferroelastic Organic Semiconductors for Ultraflexible Single-Crystal Electronics. *Angew. Chem., Int. Ed.* **2020**, *59*, 13004.
(24) Skoko, Z.; Zamir, S.; Naumov, P.; Bernstein, J. The thermosalient phenomenon."jumping crystals" and crystal chemistry of the anticholinergic agent oxitropium bromide. *J. Am. Chem. Soc.* **2010**, *132*, 14191−14202.
(25) Diao, Y.; Lenn, K. M.; Lee, W. Y.; Blood-Forsythe, M. A.; Xu, J.; Mao, Y.; Kim, Y.; Reinspach, J. A.; Park, S.; Aspuru-Guzik, A.; Xue, G.; Clancy, P.; Bao, Z.; Mannsfeld, S. C. Understanding polymorphism in organic semiconductor thin films through nanoconfinement. *J. Am. Chem. Soc.* **2014**, *136*, 17046−17057.
(26) Dickey, J. M.; Paskin, A. Computer Simulation of the Lattice Dynamics of Solids. *Phys. Rev.* **1969**, *188*, 1407−1418.
(27) Nyman, J.; Day, G. M. Static and lattice vibrational energy differences between polymorphs. *CrystEngComm* **2015**, *17*, 5154−5165.
(28) Zhang, F.; Wang, H. W.; Tominaga, K.; Hayashi, M. Characteristics of Low-Frequency Molecular Phonon Modes Studied by THz Spectroscopy and Solid-State ab Initio Theory: Polymorphs I and III of Diflunisal. *J. Phys. Chem. B* **2016**, *120*, 1698−1710.
(29) Bogdanoff, P. D.; Fultz, B. The role of phonons in the thermodynamics of the martensitic transformation in NiTi. *Philos. Mag. B* **2001**, *81*, 299−311.
(30) Wollants, P.; De Bonte, M.; Roos, J. Thermodynamic analysis of the stress-induced martensitic-transformation in a single-crystal. *Z. Metallkd.* **1979**, *70*, 113−117.
(31) Halliday, D.; Resnick, R.; Krane, K. S. *Physics*; Jon Wiley & Sons, Inc.: Hoboken, NJ, 2010; pp 600−602.
(32) Giri, G.; Verploegen, E.; Mannsfeld, S. C.; Atahan-Evrenk, S.; Kim, D. H.; Lee, S. Y.; Becerril, H. A.; Aspuru-Guzik, A.; Toney, M. F.; Bao, Z. Tuning charge transport in solution-sheared organic semiconductors using lattice strain. *Nature* **2011**, *480*, 504−508.
(33) Niewczas, M. *Dislocations in solids*; Nabarro, F. R. N., Hirth, J. P., Eds.; Elsevier B.V.: Amsterdam, 2007; pp 263−364.
(34) Hall, E. Some observations on the crystallography of deformation twins. *Acta Crystallogr.* **1953**, *6*, 570−571.
(35) Volterra, V. Sur l'équilibre des corps élastiques multiplement connexes. *Ann. Sci. École Norm. Sup.* **1907**, *24*, 401−517.
(36) Fan, C. Disclination lines in liquid crystals. *Phys. Lett. A* **1971**, *34*, 335−336.
(37) Chandrasekhar, S.; Ranganath, G. The structure and energetics of defects in liquid crystals. *Adv. Phys.* **1986**, *35*, 507−596.
(38) Olson, G. B.; Cohen, M. A general mechanism of martensitic nucleation: Part I. General concepts and the FCC→ HCP transformation. *Metall. Trans. A* **1976**, *A7*, 1897−1904.
(39) Plimpton, S. Fast parallel algorithms for short-range molecular dynamics. *J. Comput. Phys.* **1995**, *117*, 1−19.
(40) Jorgensen, W. L.; Maxwell, D. S.; Tirado-Rives, J. Development and testing of the OPLS all-atom force field on conformational energetics and properties of organic liquids. *J. Am. Chem. Soc.* **1996**, *118*, 11225−11236.
(41) Meyers, M. A.; Chawla, K. K. *Mechanical behavior of materials*; Prentice Hall: NJ, 1999; pp 66−75.
(42) Li, Y.; Li, H.; Pickard, F. C. T.; Narayanan, B.; Sen, F. G.; Chan, M. K. Y.; Sankaranarayanan, S.; Brooks, B. R.; Roux, B. Machine Learning Force Field Parameters from Ab Initio Data. *J. Chem. Theory Comput.* **2017**, *13*, 4492−4503.
(43) Li, J.; Tomkinson, J. *Theoretical and Computational Chemistry*; Elsevier: Amsterdam, 1999; pp 471−532.

https://dx.doi.org/10.1021/acs.chemmater.1c00080
Chem. Mater. 2021, 33, 1883−1892